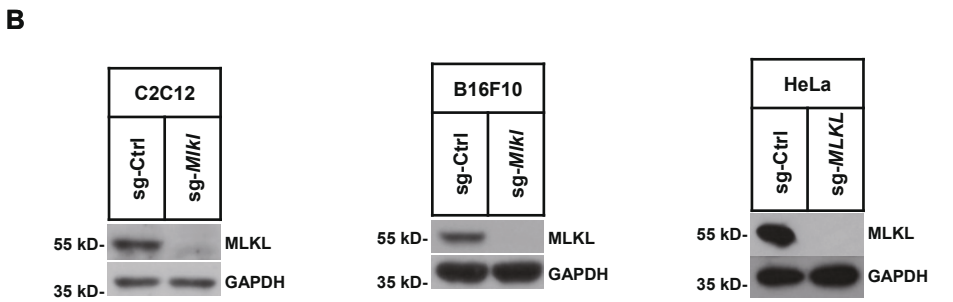
Developmental Cell, Volume *61*

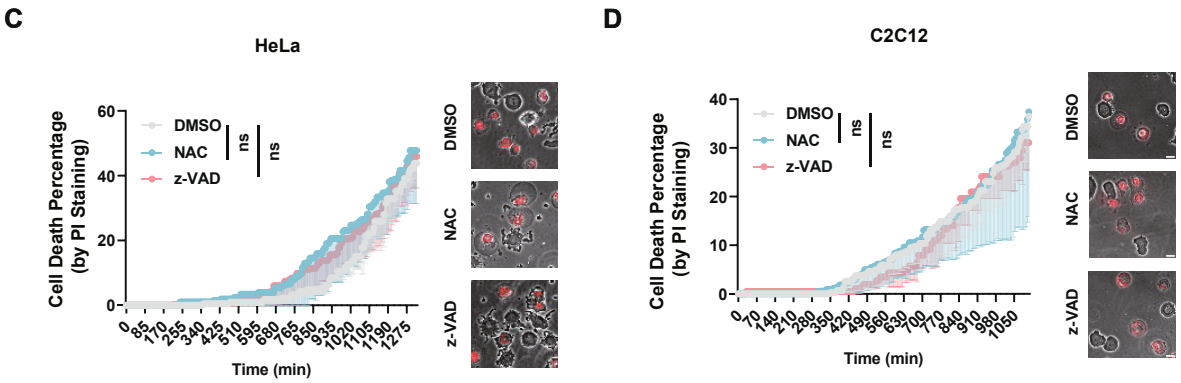
Supplemental information

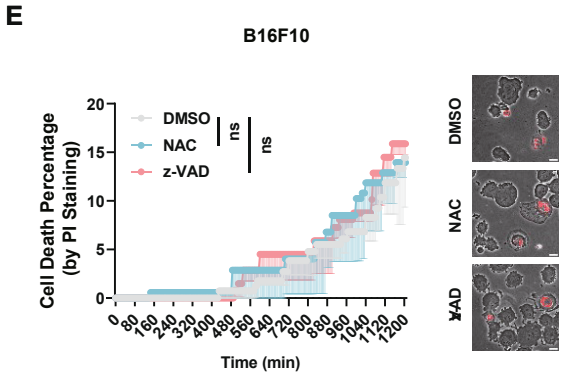
Long-term confinement triggers RIPK3-independent necroptosis in amoeboid cancer cells to shape tumor evolution

Wei Zhang, Ya-Jun Wang, Chunman Zuo, Junyi He, Xuying Ma, Haoran Wu, Bao-Qiong Lan, Dehui Kong, Luonan Chen, Gang Wei, Na Yang, Yuandi Fu, Dan Liu, Yan-Jun Liu, and Liming Sun









Supplementary Figure 1 | Validation of MLKL-dependent necroptosis following L-MAT across cell lines and controls, related to Figure 1.

Supplementary Figure 1 | Validation of MLKL-dependent necroptosis under L-MAT across cell lines and controls, related to Figure 1.

(A) Representative immunohistochemical staining of MLKL in subcutaneous tumors formed by control (sg-Ctrl) or *Mlkl*-knockout (sg-*Mlkl*) B16F10 cells. MLKL signal (brown) is counterstained with hematoxylin (blue). Red dashed lines demarcate high MLKL signal zones; green dashed lines demarcate low MLKL signal zones.

(B) Quantification of cell density in high versus low MLKL signal zones (upper panel). Cell density (cells/mm²) was determined from defined- size imaging fields using watershed segmentation with size- range exclusion by imageJ, followed by manual verification. Tissue slice thickness was 5 μm.

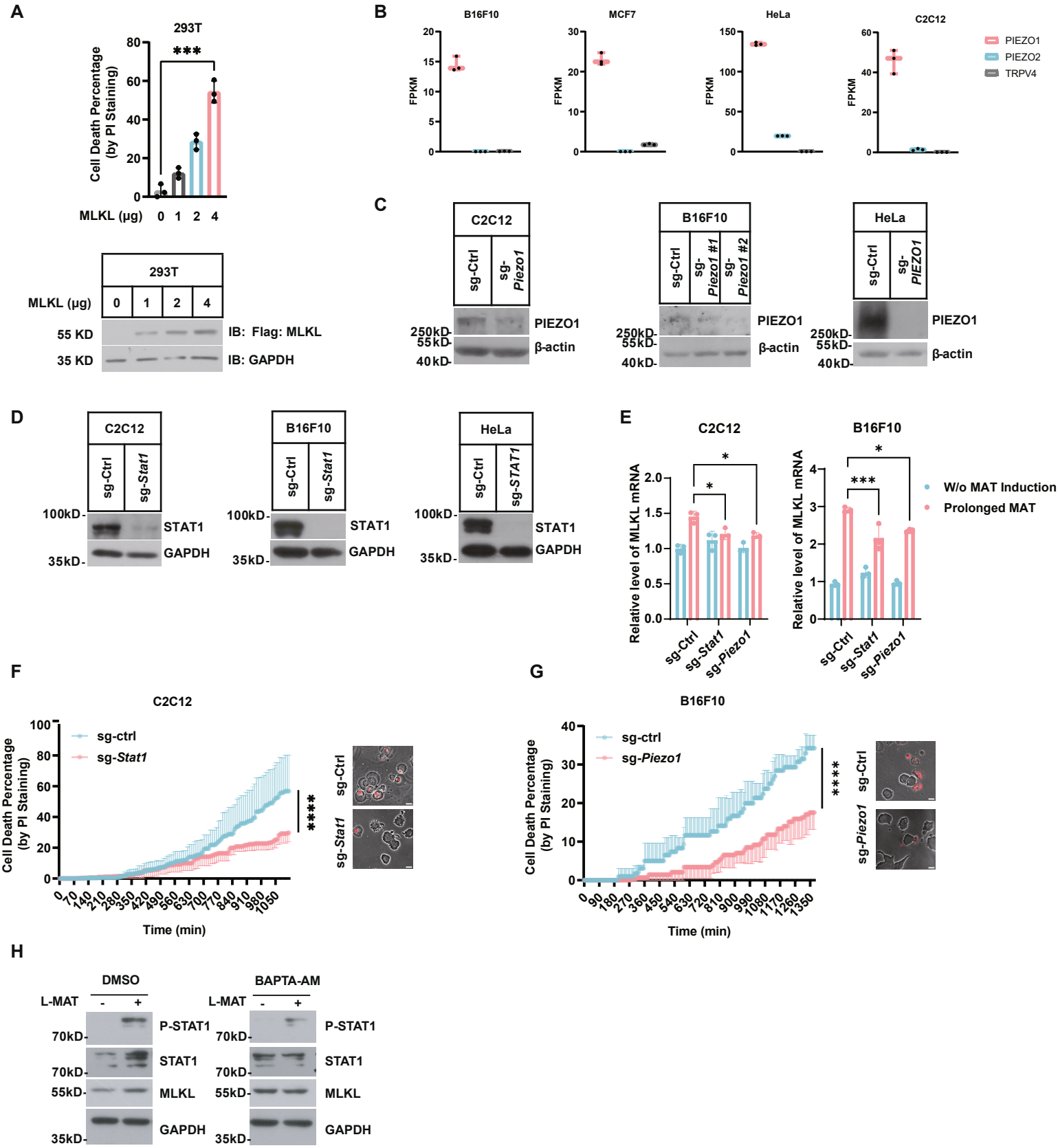
(C) Pearson correlation analysis between cell density and MLKL intensity from (A) (lower panel).

(D)GO enrichment analysis revealed that differentially expressed genes in L-MAT–tre ated HeLa cells were significantly enriched in pathways governing core cellular behav ior & signaling, including cell death and cell adhesion.

(E) Immunoblot analysis confirming MLKL knockout efficiency in indicated cell lines.

(F–H) Neither ROS inhibition nor apoptosis inhibition prevents L-MAT-induced cell death. Time course quantification of cell death following treatment with the ROS inhibitor N-acetylcysteine (NAC) or the apoptosis inhibitor z-VAD (20 μM) in HeLa (E), C2C12 (F), and B16F10 (G) cells. Representative images show PI-positive cells indicating plasma membrane rupture. Scale bar, 20 μm.

Bars show **mean ± SD**; individual dots represent single cells. Statistical analysis was performed using unpaired two-tailed Student's t-test with Welch's correction. ****P < 0.0001; ns, not significant. All experiments were repeated ≥3 independent times with consistent results; statistical analysis was conducted on pooled replicate data.



Supplementary Figure 2 | Piezo1–STAT1 signaling drives MLKL upregulation and necroptotic cell death following L-MAT, related to Figure 2.

Supplementary Figure 2 | Piezo1–STAT1 signaling drives MLKL upregulation and necroptotic cell death following L-MAT, related to Figure 2.

(A) MLKL overexpression is sufficient to induce cell death. HEK293T cells were transfected with increasing doses of MLKL-encoding plasmid. Upper panel: cell viability assessed by ATP luminescence assay. Lower panel: immunoblot analysis of MLKL expression.

(B) RNA-seq analysis indicates that *PIEZO2* and *TRPV4* are minimally expressed across the cell lines examined, suggesting they do not contribute to L-MAT-induced necroptosis.

(C) Immunoblot analysis confirming PIEZO1 knockout efficiency in the indicated cell lines.

(D) Immunoblot analysis confirming STAT1 knockout efficiency in the indicated cell lines.

(E) *Piezo1* and *Stat1* are required for L-MAT-induced *Mlkl* upregulation in murine cells. *Mlkl* mRNA levels were quantified by RT-qPCR in control, *Stat1*-knockout, or *Piezo1*-knockout C2C12 and B16F10 cells following L-MAT induction. All samples were measured within the same batch. Expression levels were normalized to *Gapdh* and presented relative to the control genotype (sg-*Ctrl*) without MAT induction as a shared reference, allowing direct statistical comparisons across all genotypes and conditions.

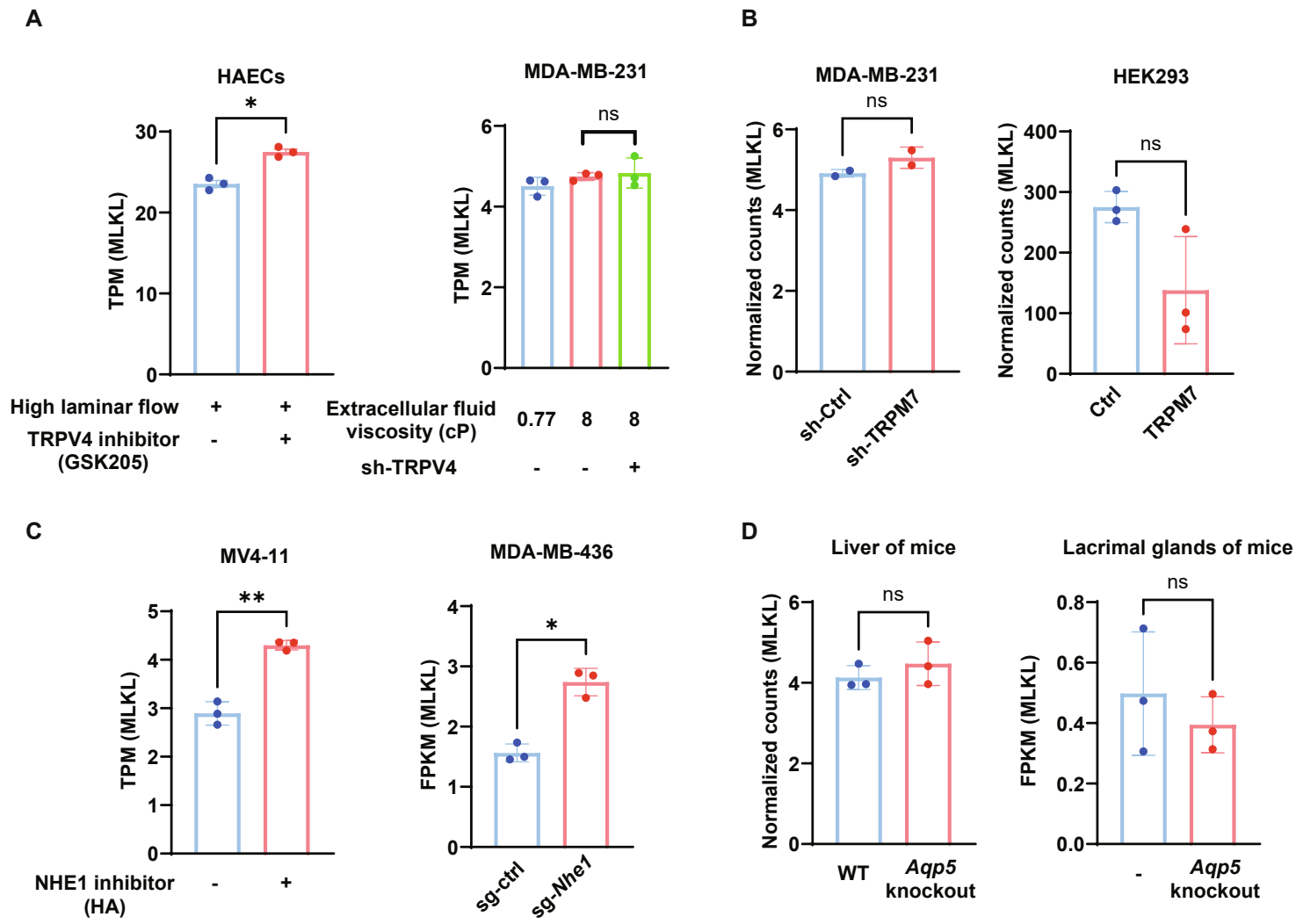
(F) *Stat1* knockout reduces L-MAT-induced cell death in C2C12 cells. Time course analysis of cell death in control (sg-Ctrl) or *Stat1*-knockout (sg-*Stat1*) C2C12 cells under MAT induction. Representative images show PI-positive cells indicating plasma membrane rupture. Scale bar, 20 μm.

(G) *Piezo1* knockout reduces L-MAT-induced cell death in B16F10 cells. Time course analysis of cell death in control (sg-Ctrl) or *Piezo1*-knockout (sg-*Piezo1*) B16F10 cells under MAT induction. Representative images show PI-positive cells indicating plasma membrane rupture. Scale bar, 20 μm.

(H) Calcium chelation suppresses L-MAT-induced STAT1 activation and MLKL upregulation. HeLa cells were pretreated with the intracellular calcium chelator BAPTA-AM (5 μM) or DMSO for 2 h, followed by L-MAT induction. Immunoblot analysis was performed to examine the levels of phosphorylated STAT1 (P-STAT1), total STAT1, and MLKL following L-MAT treatment. GAPDH served as a loading

control.

Bars depict mean ± SD; dots represent individual replicates or single cells, depending on assay. Statistical analysis was performed using one-way ANOVA followed by Tukey's multiple comparisons test for comparisons in (A), and two-way ANOVA followed by Sidak's multiple comparisons test for comparisons in (E, F, and G). *P < 0.05, ***P < 0.001, ****P < 0.0001. All experiments were repeated at least three independent times with consistent results; statistics were calculated from pooled replicate data.



Supplementary Figure 3 | Inhibition or knockout of other mechanosensitive ion channels does not inhibit MLKL transcription, related to Figure 2.

Supplementary Figure 3 | Inhibition or knockout of other mechanosensitive ion channels does not inhibit MLKL transcription, related to Figure 2.

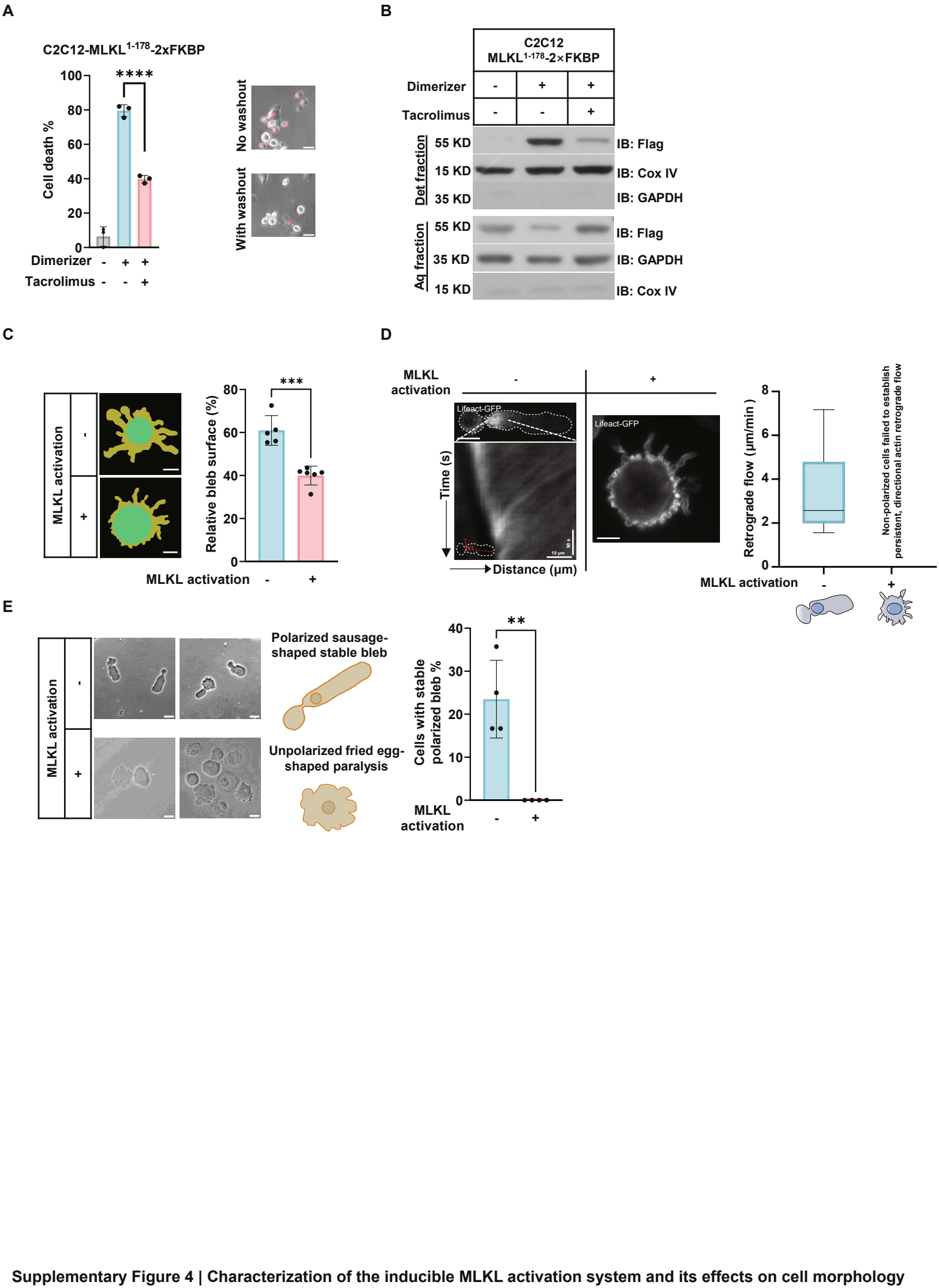
(A) TRPV4 inhibition does not inhibit MLKL transcription. Left panel: MLKL transcript levels (TPM) in human aortic endothelial cells (HAECs) under laminar flow treated with the TRPV4 antagonist GSK205 versus control (GSE255770). Right panel: MLKL transcript levels (TPM) in sh-Ctrl versus sh-*TRPV4* MDA-MB-231 cells cultured at 0.77 cP or 8 cP viscosity (GSE203651).

(B) TRPM7 modulation does not affect MLKL expression. Left panel: MLKL expression (normalized signal intensity) following *TRPM7* knockdown (GSE63956). Right panel: MLKL expression (normalized signal intensity) in control versus *TRPM7*-overexpressing HEK cells (GSE23102).

(C) NHE1 inhibition or knockout does not inhibit MLKL expression. Left panel: MLKL transcript levels (TPM) in MV4-11 cells treated with NHE1 inhibitor for 48 hours (GSE247175). Right panel: MLKL transcript levels (TPM) in control versus *NHE1*-knockout MDA-MB-436 cells (GSE270232).

(D) *Aqp5* knockout does not affect MLKL expression. Left panel: MLKL transcript levels (normalized counts) in liver tissue from wild-type versus $Aqp5^{-/-}$ mice post-partial hepatectomy (PHx) (GSE284995). Right panel: MLKL transcript levels (FPKM) in lacrimal gland tissue from wild type versus $Aqp5^{-/-}$ mice (GSE149832).

n represents the number of biological samples/groups in each dataset as deposited in GEO. Bars indicate mean ± SD; individual dots represent values from each biological replicate/sample. Statistical analysis was performed using unpaired two-tailed Student's t-test with Welch's correction. *P < 0.05, **P < 0.01, ns, not significant. Statistical computations used all available replicate values from the original datasets; no representative subset was used.



Supplementary Figure 4 | Characterization of the inducible MLKL activation system and its effects on cell morphology and cytoskeletal dynamics during MAT, related to Figure 3.

Supplementary Figure 4 | Characterization of the inducible MLKL activation system and its effects on cell morphology and cytoskeletal dynamics during MAT, related to Figure 3.

(A) Necroptosis can be halted by competitive washout of the MLKL dimerizer, enabling extended monitoring of migration behavior. C2C12-MLKL(1–178)-2×FKBP cells were treated with 10 nM dimerizer (AP20187) to induce MLKL activation until cell detachment, followed by 10 μM tacrolimus to inhibit further MLKL activation. Cell viability was assessed by ATP levels during necroptosis.

(B) MLKL membrane translocation is attenuated by dimerizer inhibition. Cell lysates were incubated at 30°C, and aqueous and detergent phases were separated. MLKL distribution between cytoplasm and plasma membrane fractions was analyzed by immunoblotting.

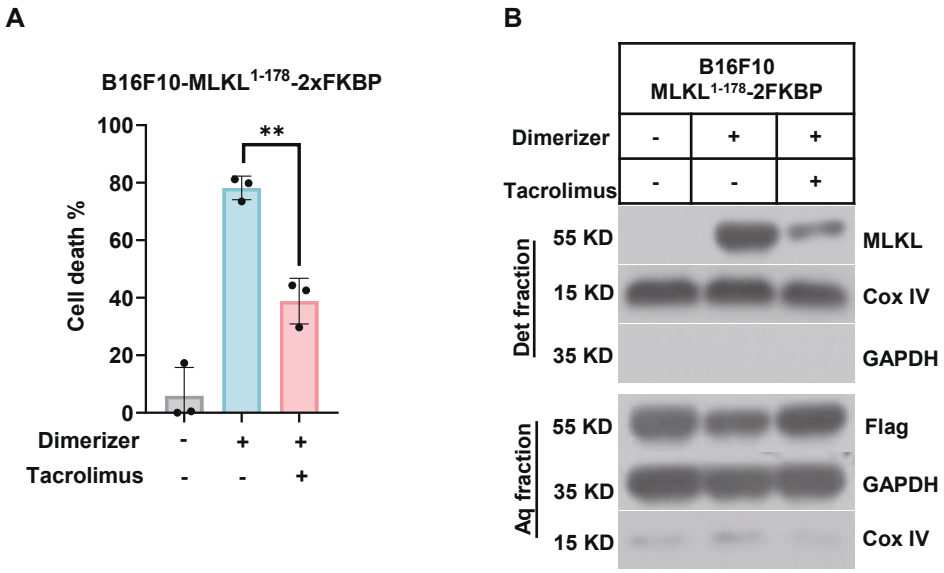
(C) MLKL-activated cells exhibit reduced blebbing activity following MAT induction. Left panel: representative images of blebbing. Right panel: quantification of bleb surface area (yellow in schematic) relative to total cell surface (green in schematic). Scale bar, 10 μm. n = 147 (non-activated) and 109 (MLKL-activated) cells.

(D) MLKL activation abolishes retrograde actin flow. Left: Representative TIRF microscopy images of actin dynamics in C2C12 cells expressing Lifeact-EGFP following MAT induction. Kymographs reveal strong retrograde flow of intracellular F-actin in non-activated cells, whereas MLKL-activated, unpolarized cells show no detectable retrograde actin flow. White dashed lines indicate cell outlines; red dashed lines indicate regions used to generate kymographs. Horizontal bars, 10 μm; vertical bars, 90 sec. Retrograde actin flow velocity was quantified from the actin kymographs shown on the left. Upon MLKL activation, cells lost polarity and failed to establish persistent directional retrograde actin flow, precluding reliable quantification of retrograde flow velocity.

(E) MLKL-activated cells fail to polarize and adopt unpolarized, fried-egg-shaped morphology following MAT induction. Non-activated cells exhibit polarized, sausage-shaped morphologies with stable blebs, whereas MLKL-activated cells form unpolarized, fried-egg-shaped structures. Left panels: representative images. Middle panels: schematic of cell morphology. Right panel: quantification. Scale bar, 20 μm. n = 73 (non-activated) and 72 (MLKL-activated) cells.

Bars indicate mean ± SD; individual dots represent each tracked cell or biological replicate as appropriate. Statistical analysis was performed using unpaired two-tailed Student’s t-test with Welch’s correction. **P < 0.01, ***P < 0.001, ****P < 0.0001,

ns, not significant. All experiments repeated at least three independent times with consistent results; statistics calculated from pooled replicate data.



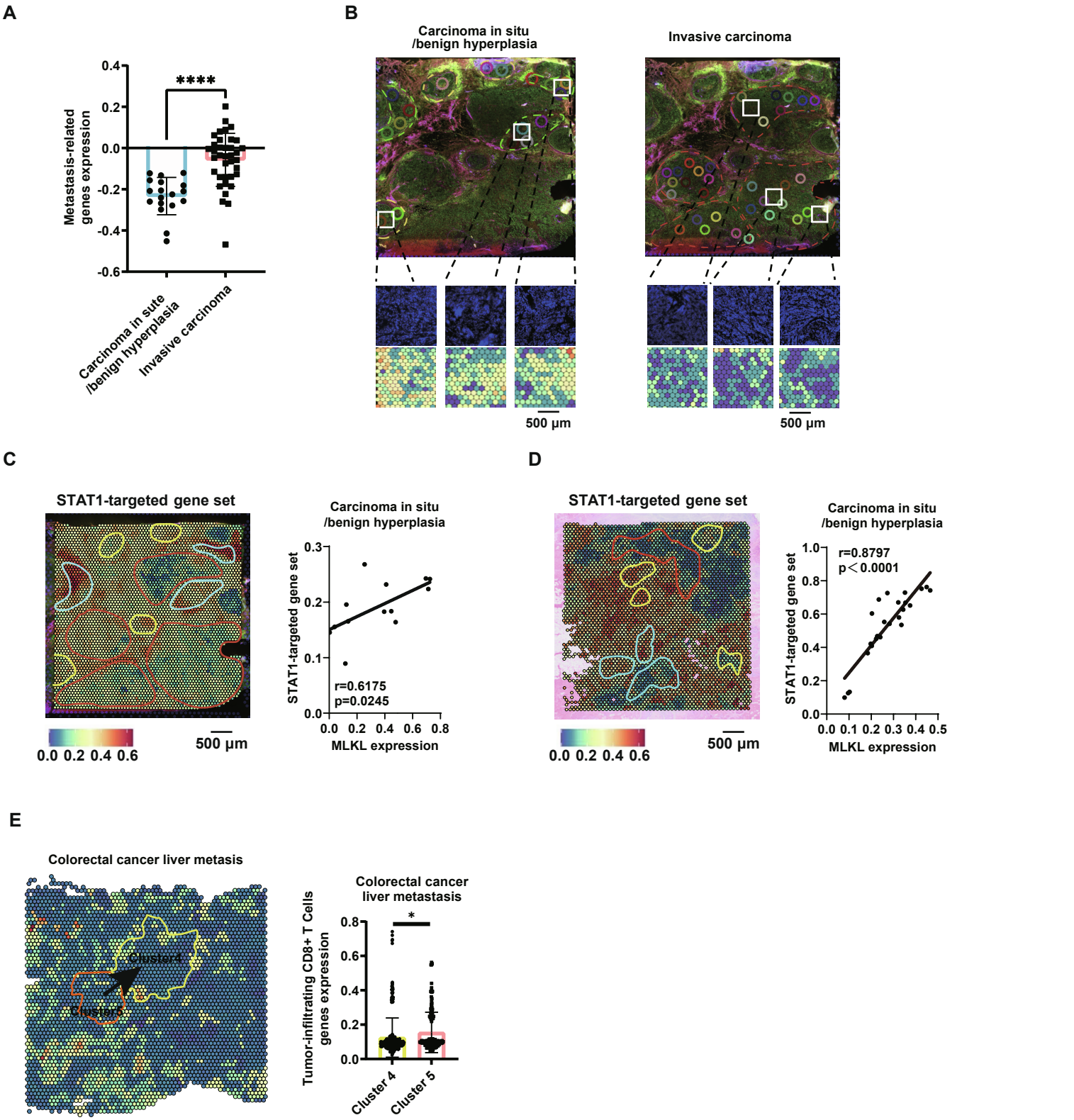
Supplementary Figure 5 | Validation of dimerizer washout strategy for controlled MLKL activation in B16F10 cells, related to Figure 4.

Supplementary Figure 5 | Validation of dimerizer washout strategy for controlled MLKL activation in B16F10 cells, related to Figure 4.

(A) Necroptosis is halted by competitive washout of the MLKL dimerizer. B16F10-MLKL(1–178)-2×FKBP cells were treated with 10 nM dimerizer (AP20187) to induce MLKL activation until cell detachment, followed by 10 μM tacrolimus to inhibit further MLKL activation. Cell viability was assessed by measuring ATP levels.

(B) Dimerizer inhibition attenuates MLKL membrane translocation. Cell lysates were incubated at 30°C, and aqueous and detergent phases were separated. MLKL distribution between cytoplasm and plasma membrane fractions was analyzed by immunoblotting.

Bars show mean ± SD; individual dots represent single cells. Statistical analysis was performed using unpaired two-tailed Student's t-test with Welch's correction. **P < 0.01. All experiments were repeated ≥3 independent times with consistent results; statistical analysis was conducted on pooled replicate data.



Supplementary Figure 6 | Additional spatial transcriptomic analyses of MLKL expression and tumor microenvironment in human cancers, related to Figure 5.

Supplementary Figure 6 | Additional spatial transcriptomic analyses of MLKL expression and tumor microenvironment in human cancers, related to Figure 5.

(A) Correlation of metastasis-related gene expression within polyclonal lesions in the IDC (Luminal B) breast cancer patient sample. Spatial expression of breast cancer metastasis related genes in carcinoma in situ/benign hyperplasia and invasive carcinoma of IDC tissue. List of breast cancer metastasis related genes were referenced from GeneCards database (https://www.genecards.org/Search/Keyword?queryString=breast%20cancer%20metastasis&sections=pathways).

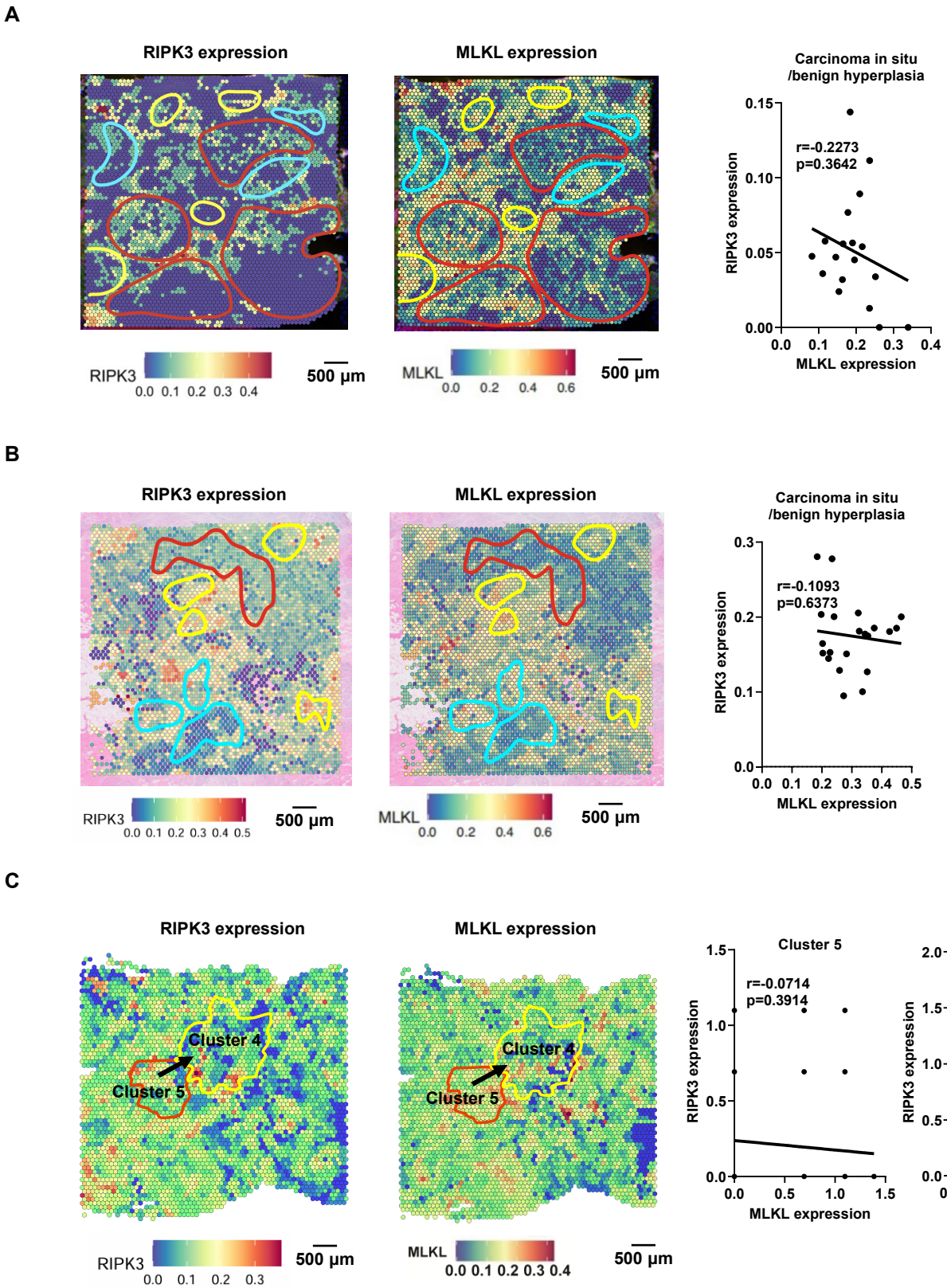
(B) Quantification of cell density and spatial MLKL expression in different zones. Circles represent selected fields for quantification analysis. DAPI staining (nuclei) was used for cell number quantification. Detailed analysis is provided in the Methods section.

(C) Spatial expression of MLKL and STAT1-targeted gene set in an invasive ductal carcinoma (IDC) breast cancer sample. Left: spatial gene expression maps of the STAT1-targeted gene set and MLKL. Right: Pearson correlation analysis reveals significant co-expression of the STAT1-targeted gene set and MLKL in the less aggressive ductal carcinoma in situ (DCIS) and benign hyperplasia regions.

(D) Spatial expression of MLKL and STAT1-targeted gene set in an FFPE-preserved breast cancer sample. Left: spatial gene expression maps of the STAT1-targeted gene set and MLKL. Right: Pearson correlation analysis reveals significant co-expression of the STAT1-targeted gene set and MLKL in the less aggressive ductal carcinoma in situ (DCIS) regions (#1 and #2).

(E) Spatial expression of tumor-infiltrating $CD8^+$ T cell-expressing genes in colorectal cancer liver metastasis tissue based on stKeep spatial clustering analysis. Left: spatial gene expression map. Right: quantification of tumor-infiltrating $CD8^+$ T cell gene expression across different regions.

n denotes independent spatial regions of interest (ROIs) within each tissue sample; numbers of ROIs for each comparison are detailed in Methods. Bars represent mean ± SD values across ROIs; each dot corresponds to a single ROI measurement. Unpaired two-tailed Student's t-test with Welch's correction. ****$P < 0.0001$. Analyses were conducted on all available ROIs pooled across ≥3 independent experiments or independent patient samples, ensuring that no single experiment was used as sole representation.



Supplementary Figure 7 | Comparison of MLKL and RIPK3 expression pattterns across human cancers, related to Figure 5.

Supplementary Figure 7 | Comparison of MLKL and RIPK3 expression patterns across human cancers, related to Figure 5.

(A) Spatial expression of RIPK3 and MLKL in an invasive ductal carcinoma (IDC) breast cancer sample. Left, spatial gene expression maps of RIPK3 and MLKL. Overall, RIPK3 expression is low throughout the tumor, particularly in the invasive carcinoma region, where MLKL expression is also relatively low. Right, Pearson correlation analysis of RIPK3 and MLKL expression in the less aggressive ductal carcinoma in situ (DCIS) and benign hyperplasia regions shows no significant correlation.

(B) Spatial expression of RIPK3 and MLKL in an FFPE-preserved breast cancer sample. Left, spatial gene expression maps of RIPK3 and MLKL. RIPK3 expression remains low, particularly within the invasive carcinoma region. Right, Pearson correlation analysis of RIPK3 and MLKL expression in the less aggressive ductal carcinoma in situ (DCIS) regions (#1 and #2) shows no significant correlation.

(C) Spatial expression of RIPK3 and MLKL in colorectal cancer with liver metastasis analyzed by stKeep-based spatial clustering. Left, spatial gene expression maps of RIPK3 and MLKL. Right, Pearson correlation analysis of RIPK3 and MLKL expression in the primary colorectal tumor (cluster 5) and liver metastatic lesion (cluster 4) shows no significant correlation.

Statistical significance for group comparisons was determined using an unpaired two-tailed Student's t-test with Welch's correction. Correlations were analyzed using the Pearson correlation coefficient.

Supplementary Table 1: GO Enrichment Analysis of L-MAT-induced HeLa Cells (related to Figure 3F)

GO ID	GO Term	Ontology	Category	Gene Ratio	Rich Factor	p-value	FDR (q-value)	z-score	Fold Enrichment	Contributing Genes
GO:0070507	regulation of microtubule cytoskeleton organization	BP	BP	136/11067		1.16625549230122e-12	2.61895970200975e-11			STMN1/STIL/PRKAA2/PATJ/SASS6/GPSM2/WDR47/PSRC1/PDE4DIP/PRUNE1/ARHGEF2/TPR/CAMSAP2/CCSAP/HNRNPU/MAPRE3/SPAST/DCTN1/CHMP3/CLASP1/TRAF3IP1/CLASP2/RHOA/PARP3/ATXN7/CHMP2B/CEP97/PHLDB2/GSK3B/CEP70/MAP6D1/TACC3/HAUS3/RNF4/SLAIN2/SNCA/TPPP/PRKAA1/MAP1B/EFNA5/APC/TRIM36/ATAT1/HSPA1A/HSPA1B/SENP6/RAC1/GNAI1/AKAP9/MET/CHMP7/CHMP4C/MAPK15/MPDZ/HAUS6/CHMP5/GBA2/BICD2/CDK5RAP2/ABL1/CAMSAP1/KIF18A/CKAP5/EML3/MARK2/ARL2/CDK2AP2/NUMA1/RPS3/PAK1/DIXDC1/PHLDB1/FKBP4/CDKN1B/BICD1/NAV3/CLIP1/SKA3/CENPJ/CKAP2/BORA/ARHGEF7/HAUS4/CHMP4A/TOGARAM1/CHMP4BP1/DYNC1H1/HAUS2/TTBK2/MAP1A/CIB1/PKD1/BMERB1/PLK1/CYLD/KATNB1/CDH5/CHMP1A/PAFAH1B1/RANGRF/SPAG5/TAOK1/GIT1/CDK5R1/MAPT/SKA2/CLTC/CHMP6/TBCD/CHMP1B/ROCK1/MAPRE2/HAUS1/SKA1/VPS4B/APC2/CAMSAP3/HAUS8/MAP1S/HAUS5/CLIP3/EML2/NUP62/CHMP2A/TPX2/MAPRE1/CHMP4B/RAE1/DYRK1A/GAS2L1/DRG1/MID1/MID1IP1/HDAC6/HAUS7/MECP2
GO:0044380	protein localization to cytoskeleton	BP	BP	57/11067		1.79754256117842e-11	3.25844958881127e-10			DVL1/KLHL21/STIL/CEP350/DISC1/HNRNPU/MAPRE3/CRIPT/GSK3B/GOLGB1/CCDC14/CEP72/APC/DIAPH1/TTK/SNX10/NUDCD3/MCPH1/PCM1/HOOK3/UBXN2B/FAM83H/ABHD17B/ABL1/KIF20B/NUMA1/C2CD3/BICD1/DCTN2/CEP83/PIBF1/CHAMP1/TTBK2/MAP1A/RAB11A/BBS4/ABHD17C/RAB11FIP3/PARD6A/KIAA0753/SPAG5/PPP1R9B/CEP131/CSNK1D/CEP192/MAPRE2/ABHD17A/MARK4/NUP62/NSFL1C/MAPRE1/CEP250/FAM83D/AURKA/GAS2L1/MID1/MID2
GO:0051495	positive regulation of cytoskeleton organization	BP	BP	136/11067		1.03453573595148e-05	6.99037068351711e-05			MTOR/ARHGEF10L/CDC42/WASF2/STIL/SASS6/GPSM2/PSRC1/RHOC/PDE4DIP/S100A10/NES/KIRREL1/PFDN2/ITGB1BP1/ROCK2/SPAST/CDC42EP3/PRKCE/CCDC88A/PLEK/DCTN1/NCK2/CLASP1/BIN1/NCKAP1/ABI2/ARPC2/BRK1/RHOA/CD47/NCK1/PFN2/DLG1/WDR1/LIMCH1/SLAIN2/CRACD/PLK4/RICTOR/MAP1B/F2RL1/FER/CEP120/FCHSD1/SYNPO/EDN1/CARMIL1/TRIM27/HSPA1A/HSPA1B/WASF1/CCN2/SNX9/RAC1/LIMK1/AKAP9/BAIAP2L1/PPP1R35/MET/BRAF/EPHA1/ARHGEF5/ARHGEF10/SORBS3/PTK2B/BAG4/MTSS1/MAPK15/TESK1/TGFBR1/CDK5RAP2/GSN/ABL1/NRP1/WASHC2C/ADD3/SWAP70/CKAP5/ARL2/CTTN/NUMA1/FCHSD2/RPS3/WNT11/PAK1/CEP295/CDKN1B/RAPGEF3/NAV3/PXN/CLIP1/CENPJ/CFL2/TOGARAM1/ARF6/FERMT2/TGFB3/EVL/DYNC1H1/CYFIP1/KATNBL1/C15orf62/TPM1/SMAD3/WHAMM/MLST8/MYLK3/KATNB1/FHOD1/CARMIL2/SERPINF2/PFN1/SPAG5/GIT1/CDK5R1/MAPT/CDC42EP4/GRB2/BAIAP2/VPS4B/NPHS1/VASP/NUP62/DSTN/MAPRE1/SDC4/PPM1F/NF2/DRG1/CDC42EP1/PDXP/BAIAP2L2/MECP2/FLNA/PLXNA3
GO:0010631	epithelial cell migration	BP	BP	221/11067		0.4033733388851229	0.5348707022067942			PLEKHG5/PIK3CD/MTOR/EPHA2/ZC3H12A/MACF1/EDN2/SVBP/PIK3R3/PLPP3/GADD45A/PKN2/S100A2/RAB13/EFNA1/GLUL/PTGS2/ADIPOR1/ATP2B4/TGFB2/DUSP10/MIA3/LGALS8/ITGB1BP1/ADAM17/ROCK2/RHOB/CYP1B1/PRKCE/RTN4/WDPCP/ATOH8/MAP4K4/EPB41L5/CLASP1/ZEB2/NFE2L2/BMPR2/NRP2/AAMP/SCG2/SP100/VHL/PPARG/IQSEC1/CAPN7/TGFBR2/CLASP2/PTPN23/GPX1/RHOA/HYAL1/WNT5A/FOXP1/ROBO1/FSTL1/GATA2/PLXND1/PIK3CB/PFN2/PDCD10/PIK3CA/S100P/FGFBP1/ANXA3/EGF/FGF2/FBXW7/PDCD6/ITGA2/PLK2/ARSB/MACIR/MCC/HBEGF/SPARC/FGF18/RREB1/EDN1/GPLD1/CSNK2B/PPARD/SRF/VEGFA/NUS1/SASH1/RAC1/ANLN/HSPB1/KRIT1/EPHB4/MET/PAXIP1/EGR3/LOXL2/DOCK5/PTK2B/ADGRA2/FGFR1/ADAM9/SNAI2/ANGPT1/CCN3/HAS2/PTK2/PTP4A3/GFUS/EPPK1/KANK1/TESK1/ANXA1/TGFBR1/KLF4/EPB41L4B/DAB2IP/PKN3/ABL1/NOTCH1/GATA3/ITGB1/NRP1/SIRT1/MMRN2/PTEN/NANOS1/DOCK1/PIK3C2A/LPXN/CORO1B/PRCP/ETS1/HDAC7/ACVRL1/NR4A1/SP1/ATP5F1B/KITLG/DCN/CORO1C/PTPN11/PXN/P2RX4/SCARB1/HMGB1/STARD13/IRS2/LTB4R2/ARHGAP5/ARF6/HIF1A/SYNJ2BP/LGMN/EVL/AKT1/SPRED1/THBS1/DLL4/FGF7/RAB11A/MAP2K5/CTSH/CIB1/NR2F2/PDPK1/EMP2/CDH5/BCAR1/PLCG2/FOXC2/SERPINF1/PFN1/MAP2K3/NF1/KRT16/JUP/STAT5A/HDAC5/GRN/ITGB3/ITGA3/BCAS3/MAP3K3/PRKCA/PTPRM/ROCK1/MAPRE2/ATP5F1A/SMAD4/TBXA2R/LRG1/KANK2/CALR/PKN1/GIPC1/GPI/TGFB1/APOE/PRKD2/FUT1/RRAS/EMC10/ZNF580/FERMT1/RIN2/ID1/SRC/PLCG1/SNAI1/SOX18/PPM1F/PATZ1/HMOX1/MYH9/CARD10/SH3BP1/PDGFB/PRKX/TMSB4X/HDAC6/SRPX2/MECP2
GO:0090130	tissue migration	BP	BP	221/11067		0.5993037755579282	0.6918332453304606			PLEKHG5/PIK3CD/MTOR/EPHA2/ZC3H12A/MACF1/EDN2/SVBP/PIK3R3/PLPP3/GADD45A/PKN2/S100A2/RAB13/EFNA1/GLUL/PTGS2/ADIPOR1/ATP2B4/TGFB2/DUSP10/MIA3/LGALS8/ITGB1BP1/ADAM17/ROCK2/RHOB/CYP1B1/PRKCE/RTN4/WDPCP/ATOH8/MAP4K4/EPB41L5/CLASP1/ZEB2/NFE2L2/BMPR2/NRP2/AAMP/SCG2/SP100/VHL/PPARG/IQSEC1/CAPN7/TGFBR2/CLASP2/PTPN23/GPX1/RHOA/HYAL1/WNT5A/FOXP1/ROBO1/FSTL1/GATA2/PLXND1/PIK3CB/PFN2/PDCD10/PIK3CA/S100P/FGFBP1/ANXA3/EGF/FGF2/FBXW7/PDCD6/ITGA2/PLK2/ARSB/MACIR/MCC/HBEGF/SPARC/FGF18/RREB1/EDN1/GPLD1/CSNK2B/PPARD/SRF/VEGFA/NUS1/SASH1/RAC1/ANLN/HSPB1/KRIT1/EPHB4/MET/PAXIP1/EGR3/LOXL2/DOCK5/PTK2B/ADGRA2/FGFR1/ADAM9/SNAI2/ANGPT1/CCN3/HAS2/PTK2/PTP4A3/GFUS/EPPK1/KANK1/TESK1/ANXA1/TGFBR1/KLF4/EPB41L4B/DAB2IP/PKN3/ABL1/NOTCH1/GATA3/ITGB1/NRP1/SIRT1/MMRN2/PTEN/NANOS1/DOCK1/PIK3C2A/LPXN/CORO1B/PRCP/ETS1/HDAC7/ACVRL1/NR4A1/SP1/ATP5F1B/KITLG/DCN/CORO1C/PTPN11/PXN/P2RX4/SCARB1/HMGB1/STARD13/IRS2/LTB4R2/ARHGAP5/ARF6/HIF1A/SYNJ2BP/LGMN/EVL/AKT1/SPRED1/THBS1/DLL4/FGF7/RAB11A/MAP2K5/CTSH/CIB1/NR2F2/PDPK1/EMP2/CDH5/BCAR1/PLCG2/FOXC2/SERPINF1/PFN1/MAP2K3/NF1/KRT16/JUP/STAT5A/HDAC5/GRN/ITGB3/ITGA3/BCAS3/MAP3K3/PRKCA/PTPRM/ROCK1/MAPRE2/ATP5F1A/SMAD4/TBXA2R/LRG1/KANK2/CALR/PKN1/GIPC1/GPI/TGFB1/APOE/PRKD2/FUT1/RRAS/EMC10/ZNF580/FERMT1/RIN2/ID1/SRC/PLCG1/SNAI1/SOX18/PPM1F/PATZ1/HMOX1/MYH9/CARD10/SH3BP1/PDGFB/PRKX/TMSB4X/HDAC6/SRPX2/MECP2
GO:0010632	regulation of epithelial cell migration	BP	BP	165/11067		0.8448074121030455	0.7084734281 15887			PIK3CD/MTOR/EPHA2/ZC3H12A/MACF1/SVBP/PLPP3/GADD45A/EFNA1/GLUL/PTGS2/ADIPOR1/ATP2B4/TGFB2/DUSP10/ITGB1BP1/ADAM17/ROCK2/RHOB/PRKCE/RTN4/ATOH8/MAP4K4/EPB41L5/CLASP1/NFE2L2/BMPR2/NRP2/AAMP/SP100/PPARG/IQSEC1/CAPN7/TGFBR2/CLASP2/PTPN23/RHOA/HYAL1/WNT5A/FOXP1/GATA2/PIK3CB/PFN2/PDCD10/FGFBP1/ANXA3/EGF/FGF2/FBXW7/PDCD6/ITGA2/PLK2/ARSB/MACIR/MCC/HBEGF/SPARC/FGF18/RREB1/EDN1/GPLD1/CSNK2B/VEGFA/NUS1/SASH1/RAC1/HSPB1/KRIT1/MET/DOCK5/PTK2B/ADGRA2/FGFR1/ADAM9/ANGPT1/HAS2/PTK2/GFUS/EPPK1/ANXA1/KLF4/EPB41L4B/DAB2IP/ABL1/NOTCH1/GATA3/NRP1/SIRT1/MMRN2/PTEN/DOCK1/PIK3C2A/PRCP/ETS1/HDAC7/ACVRL1/SP1/ATP5F1B/DCN/CORO1C/P2RX4/SCARB1/HMGB1/STARD13/IRS2/ARHGAP5/ARF6/HIF1A/SYNJ2BP/LGMN/EVL/AKT1/SPRED1/THBS1/DLL4/FGF7/RAB11A/MAP2K5/CTSH/CIB1/NR2F2/PDPK1/EMP2/BCAR1/PLCG2/FOXC2/SERPINF1/PFN1/MAP2K3/NF1/JUP/STAT5A/HDAC5/GRN/ITGB3/ITGA3/BCAS3/MAP3K3/PRKCA/PTPRM/MAPRE2/ATP5F1A/TBXA2R/CALR/GPI/TGFB1/APOE/PRKD2/FUT1/RRAS/EMC10/ZNF580/RIN2/SRC/PLCG1/PPM1F/PATZ1/HMOX1/CARD10/SH3BP1/PDGFB/TMSB4X/HDAC6/SRPX2/MECP2
GO:0044331	cell-cell adhesion mediated by cadherin	BP	BP	21/11067		0.9870414664 07548	0.7084734281 15887			MAD2L2/PTPRU/WNT5A/DENND6A/CDH10/FER/BMP6/FLOT1/VEGFA/AFDN/NOTCH1/PLEKHA7/CTNND1/CDH24/FOXA1/TJP1/CDH5/CDH1/SERPINF2/MMP24/PPM1F
GO:0043534	blood vessel endothelial cell migration	BP	BP	88/11067		0.9975110087 76293	0.7084734281 15887			EPHA2/PIK3R3/GADD45A/EFNA1/PTGS2/ATP2B4/MIA3/ITGB1BP1/ADAM17/CYP1B1/NFE2L2/VHL/PPARG/GPX1/RHOA/ROBO1/GATA2/PDCD10/FGFBP1/FGF2/FBXW7/PLK2/FGF18/GPLD1/CSNK2B/SRF/VEGFA/NUS1/HSPB1/EPHB4/EGR3/PTK2B/FGFR1/ANGPT1/ANXA1/KLF4/ABL1/NOTCH1/ITGB1/NRP1/SIRT1/MMRN2/PIK3C2A/PRCP/ETS1/HDAC7/ACVRL1/NR4A1/SP1/ATP5F1B/P2RX4/SCARB1/HMGB1/STARD13/HIF1A/AKT1/SPRED1/THBS1/DLL4/MAP2K5/CIB1/PDPK1/EMP2/CDH5/FOXC2/MAP2K3/NF1/JUP/STAT5A/HDAC5/MAP3K3/PRKCA/ATP5F1A/TBXA2R/TGFB1/APOE/PRKD2/ID1/PLCG1/SOX18/HMOX1/MYH9/CARD10/SH3BP1/PDGFB/TMSB4X/SRPX2/MECP2
GO:0060326	cell chemotaxis	BP	BP	142/11067		0.9999999837 19981	0.7084734281 15887			ARHGEF16/PLEKHG5/PIK3CD/EPHA2/NBL1/AKIRIN1/EDN2/PDE4B/VAV3/PIP5K1A/S100A14/RAB13/IL6R/TGFB2/LYST/ADAM17/CXCR4/PIKFYVE/SCG2/CCL20/PRSS56/ACKR3/IL17RC/OXSR1/CCR3/PRKCD/WNT5A/CXCL8/PF4V1/PF4/PPBP/CXCL5/CXCL3/CXCL2/FGF2/GAB1/HMGB2/ITGA1/F2RL1/LOX/SLC12A2/HBEGF/CSF1R/PDGFRB/CD74/FGF18/DUSP1/NEDD9/EDN1/VEGFA/TPBG/RAC1/IL6/PPIA/SBDS/HSPB1/SERPINE1/DOCK4/MET/ARHGEF5/MTUS1/EGR3/PTK2B/FGFR1/LYN/CCN3/PTK2/PLEC/CREB3/ANXA1/NINJ1/C5/NOTCH1/CAMK1D/NRP1/MCU/GBF1/ADAM8/RHOG/SWAP70/PARVA/MDK/VEGFB/CORO1B/TIRAP/WNK1/DNM1L/ANO6/BIN2/NR4A1/SLC8B1/P2RX4/HMGB1/GAS6/SRP54/LGALS3/LGMN/THBS1/ADAM10/DAPK2/PPIB/ABCC1/MAPK3/HSD3B7/BCAR1/CRK/ARRB2/C1QBP/TMEM102/LGALS9/CCL2/MMP28/CCL5/NUP85/RAC3/TNFRSF11A/BSG/PIP5K1C/VAV1/CALR/ADGRE2/RPS19/PRKD2/C5AR1/C5AR2/TRPM4/RPL13A/ZNF580/ELMO2/PREX1/CXADR/TRPM2/ITGB2/IL17RA/CRKL/MAPK1/DDT/PDGFB/TMSB4X/MOSPD2/PLXNB3/MPP1

Supplementary Table 1 | GO Enrichment Analysis of L-MAT-induced HeLa Cells, related to Figure 3F.

Supplementary Table 2: Differentially Expressed Genes in Enriched Pathways (related to Figure 3G)

Gene Symbol	Gene Name	log_2FC	p-value	Associated GO Terms
RHOA	RHOA	-0.0110	3.70e-11	regulation of microtubule cytoskeleton organization
RAC1	RAC1	0.1853	3.70e-11	regulation of microtubule cytoskeleton organization
MET	MET	-0.2105	3.70e-11	regulation of microtubule cytoskeleton organization
ABL1	ABL1	0.2590	3.70e-11	regulation of microtubule cytoskeleton organization
MECP2	MECP2	-0.1367	3.70e-11	regulation of microtubule cytoskeleton organization
ABL1	ABL1	0.2590	4.60e-10	protein localization to cytoskeleton
RHOA	RHOA	-0.0110	9.87e-05	positive regulation of cytoskeleton organization
RAC1	RAC1	0.1853	9.87e-05	positive regulation of cytoskeleton organization
MET	MET	-0.2105	9.87e-05	positive regulation of cytoskeleton organization
PTK2B	PTK2B	-0.4332	9.87e-05	positive regulation of cytoskeleton organization
ABL1	ABL1	0.2590	9.87e-05	positive regulation of cytoskeleton organization
NRP1	NRP1	-0.2914	9.87e-05	positive regulation of cytoskeleton organization
MECP2	MECP2	-0.1367	9.87e-05	positive regulation of cytoskeleton organization
ADAM17	ADAM17	0.3796	0.755	epithelial cell migration
RHOA	RHOA	-0.0110	0.755	epithelial cell migration
VEGFA	VEGFA	1.1989	0.755	epithelial cell migration
RAC1	RAC1	0.1853	0.755	epithelial cell migration
MET	MET	-0.2105	0.755	epithelial cell migration
PTK2B	PTK2B	-0.4332	0.755	epithelial cell migration
ABL1	ABL1	0.2590	0.755	epithelial cell migration
NOTCH1	NOTCH1	0.1728	0.755	epithelial cell migration
NRP1	NRP1	-0.2914	0.755	epithelial cell migration
MECP2	MECP2	-0.1367	0.755	epithelial cell migration
ADAM17	ADAM17	0.3796	0.977	tissue migration
RHOA	RHOA	-0.0110	0.977	tissue migration
VEGFA	VEGFA	1.1989	0.977	tissue migration
RAC1	RAC1	0.1853	0.977	tissue migration
MET	MET	-0.2105	0.977	tissue migration
PTK2B	PTK2B	-0.4332	0.977	tissue migration
ABL1	ABL1	0.2590	0.977	tissue migration
NOTCH1	NOTCH1	0.1728	0.977	tissue migration
NRP1	NRP1	-0.2914	0.977	tissue migration
MECP2	MECP2	-0.1367	0.977	tissue migration
ADAM17	ADAM17	0.3796	1.000	regulation of epithelial cell migration
RHOA	RHOA	-0.0110	1.000	regulation of epithelial cell migration
VEGFA	VEGFA	1.1989	1.000	regulation of epithelial cell migration
RAC1	RAC1	0.1853	1.000	regulation of epithelial cell migration
MET	MET	-0.2105	1.000	regulation of epithelial cell migration
PTK2B	PTK2B	-0.4332	1.000	regulation of epithelial cell migration
ABL1	ABL1	0.2590	1.000	regulation of epithelial cell migration
NOTCH1	NOTCH1	0.1728	1.000	regulation of epithelial cell migration
NRP1	NRP1	-0.2914	1.000	regulation of epithelial cell migration
MECP2	MECP2	-0.1367	1.000	regulation of epithelial cell migration
VEGFA	VEGFA	1.1989	1.000	cell-cell adhesion mediated by cadherin
NOTCH1	NOTCH1	0.1728	1.000	cell-cell adhesion mediated by cadherin
ADAM17	ADAM17	0.3796	1.000	blood vessel endothelial cell migration
RHOA	RHOA	-0.0110	1.000	blood vessel endothelial cell migration
VEGFA	VEGFA	1.1989	1.000	blood vessel endothelial cell migration
PTK2B	PTK2B	-0.4332	1.000	blood vessel endothelial cell migration
ABL1	ABL1	0.2590	1.000	blood vessel endothelial cell migration
NOTCH1	NOTCH1	0.1728	1.000	blood vessel endothelial cell migration
NRP1	NRP1	-0.2914	1.000	blood vessel endothelial cell migration
MECP2	MECP2	-0.1367	1.000	blood vessel endothelial cell migration
ADAM17	ADAM17	0.3796	1.000	cell chemotaxis
VEGFA	VEGFA	1.1989	1.000	cell chemotaxis
RAC1	RAC1	0.1853	1.000	cell chemotaxis
MET	MET	-0.2105	1.000	cell chemotaxis
PTK2B	PTK2B	-0.4332	1.000	cell chemotaxis
NOTCH1	NOTCH1	0.1728	1.000	cell chemotaxis
NRP1	NRP1	-0.2914	1.000	cell chemotaxis

Supplementary Table 2 | Differentially Expressed Genes in Enriched Pathways, related to Figure 3G.

Supplementary Table 3: Analysis Parameters and Software (related to Figure 1C and supplementary Figure 2B)

Parameter	Value/Setting
Analysis software	DESeq2
R version	4.3.1
Organism database	hg38
Background gene set	All expressed genes after filtering
Statistical test	Wald test (negative binomial model)
Multiple testing correction	Benjamini–Hochberg (BH)
p-value cutoff	0.05
FDR cutoff	0.05
Minimum gene count	≥10 reads across three samples
Visualization package	ggplot2 (with ggrepel, dplyr)

Supplementary Table 3 | Analysis Parameters and Software1222, related to Figure 1C and Supplementary Figure 2B.